Advanced Imaged-based Workflow for 3D Pore Surface Roughness Quantification

Yiteng Li[1,*], *Xupeng He*[2], *Hyung Kwak*[2], and *Hussein Hoteit*[1]

[1]Ali I. Al-Naimi Petroleum Engineering Research Center, King Abdullah University of Science and Technology, 23955 Thuwal, Saudi Arabia
[2]EXPEC ARC, Saudi Aramco, 34466 Dhahran, Saudi Arabia

Abstract. Surface roughness is a scale-dependent property and it is defined and characterized at different length scales depending on the application. When simulating nuclear magnetization decay in digital rocks, the irregular pore geometry, acting as the visible "roughness", accelerates surface relaxation and shortens T2 relaxation time. To accurately characterize pore structures from NMR T2 responses, the surface roughness effect must be considered; on top of that, it is necessary to characterize and quantify surface roughness. In this study, an innovative pore surface roughness characterization workflow is proposed to directly characterize 3D surface roughness from segmented μ-CT images. A two-level pore separation algorithm divides the connected pore structure into separated pore bodies to ease the surface reconstruction step. The pore surface is reconstructed by the combination of spherical parameterization and spherical harmonic (SH) expansion, producing a set of SH coefficients, which are then used to build the reference surface. We then define the local roughness at each vertex of the reference surface, and a 3D surface roughness coefficient is calculated by weighted averaging of all the local roughness over the reference surface. Numerical results show that the combination of spherical parameterization and SH expansion provides a technologically feasible approach to characterize the surface roughness of pore structures in 3D space.

1. Introduction

Surface roughness is a persistent challenge in the petroleum industry that may significantly influence the determination of reservoir rock properties such as pore sizes and contact angles [1, 2]. As one of the NMR logging measurements, T2 relaxation times are correlated with the pore structure within the fast diffusion regime [3]. When interpreting pore sizes from NMR T2 responses, the analytical solution assumes idealized pore shapes with smooth surfaces [4]. Under this circumstance, the surface relaxivity becomes an adjustable parameter to characterize pore sizes, which shows its own drawback in reliably calculating pore size distributions [5]. Moreover, this treatment overlooks the effect of irregular pore shapes and surface roughness on NMR T2 relaxation; as a result, pore sizes are often underestimated [2, 6, 7, 8]. To correctly characterize pore structures from T2 relaxation times, it is necessary to account for these geometry effects. This requires practical methods to accurately characterize pore shape irregularity and surface roughness in 3D space.

Typically, surface roughness is measured in the laboratory using sophisticated microscopes, such as atomic force microscopy and laser scanner confocal microscopy [2, 6]. These instruments measure surface roughness on a cross-section plane of the rock sample, producing high-precision measurements after filtering out the pore-shape/pore-size effect. However, these methods are restrictive to 2D planar regions and cannot characterize the 3D surface roughness.

Micro-computed tomography (μ-CT) is a 3D imaging technique to digitize rock core plugs into greyscale image. The produced greyscale data, after proper image segmentation, have been used to numerically investigate the pore structure of digital rock by simulating NMR T2 relaxation [9, 10]. Since the length scale of surface roughness is much smaller than the image resolution, μ-CT images cannot resolve the actual surface roughness. However, the irregular pore geometry, which is removed from laboratory measurements, now plays a critical role in accelerating surface relaxation and shortening T2 relaxation time [7, 8]. From the macroscopic point of view, the irregularity of pore shapes acts as the "surface roughness" that is visible from micro-CT images. Thus, we want to seek an approach to effectively characterize and quantify this geometry effect for improving the reliability of pore structure characterization from NMR T2 simulation.

It is nontrivial to directly characterize pore surface roughness in 3D space. To reduce the computational difficulty, last year Li et al. adopted a dimension reduction strategy to decompose a synthetic 3D pore volume into a plurality of 2D cross-sectional images [8]. The overall surface roughness was parameterized into a dimensionless number by weighted averaging of the pore roughness coefficients of all the cross-sectional images. This method only considers the morphological features of 2D cross sections, and it works under a strong assumption that the morphological features of 2D cross-sectional images do not much differ from the morphological features of the 3D pore volume. This restricts

* Corresponding author: yiteng.li@kaust.edu.sa

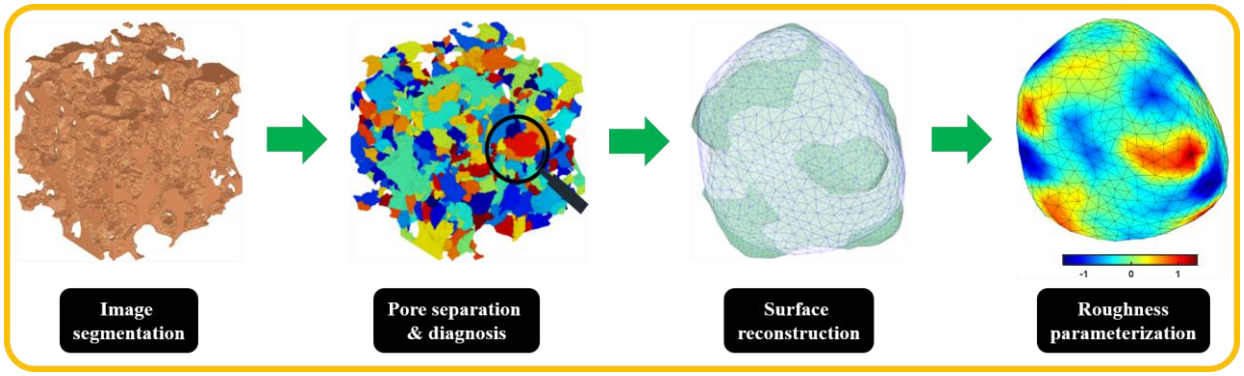

Fig. 1. Schematic diagram of 3D pore surface roughness characterization workflow using spherical harmonics.

the application of their method to more complicated pore structures

To resolve the aforementioned issues, this study develops an image-based workflow using spherical harmonics to directly characterize 3D pore surface roughness. Spherical harmonics are a shape descriptor particularly suited to model arbitrarily shaped but simply connected 3D objects [11]. It has been successfully applied to multiple areas, including computer vision [12] and medical image analysis [13, 14]. This class of methods creates an orthogonal basis to mathematically represent the 3D object surface [15]. Therefore, the morphology of the reconstructed surface is controlled by the number of spherical harmonic (SH) series. The reconstructed surface exhibits more surface textures with increasing the number of SH basis functions, while it preserves a general shape if only a few spherical harmonics are used. This characteristic enables us to calculate SH coefficients by fitting the pore surface and utilize a subset of coefficients to build the reference surface for roughness characterization and quantification. Inspired by this, we propose an innovative workflow combining spherical parameterization and SH expansion for direct characterization of 3D pore surface roughness. The proposed workflow includes four main steps, including image segmentation, pore separation and diagnosis, surface reconstruction, and roughness parameterization. Numerical results show that the combination of spherical parameterization and SH expansion provides a technologically feasible approach to characterize the surface roughness of pore structures in 3D space.

2. 3D pore surface roughness characterization

The proposed workflow includes four main steps, as shown in **Fig. 1**. The key to success is calculating proper SH basis functions to reproduce the pore surface. Then a subset of SH coefficients is then used to build the reference surface from which the local roughness is defined and characterized. Since image segmentation is not our focus in this study, we will detail the remaining steps of the proposed workflow in the following of this section.

2.1. Image segmentation

This step converts the grayscale μ-CT image into the binary volume where pore voxels are 1 and solid voxels are 0. Before segmentation, some preprocessing steps are conducted, including volume editing and calibration, image denoising, and subvolume extraction. The segmented image is cleaned by removing isolated tiny pores and solids.

2.2. Pore separation and diagnosis

The second step aims to divide the connected pore structures into a number of disconnected pore bodies to reduce the computational difficulty of the surface reconstruction step, as the entire pore space is too complicated to be modeled by any of the shape descriptors. In particular, watershed segmentation is a popular approach to segmenting individual objects that constitute an aggregated structure. It is extensively used to separate pores for pore network extraction and segment grains for shape analysis [16-18]. The basic idea behind watershed segmentation methods is to convert the objects of interest to catchment basins with regional maximum depths (equivalent to regional minimum numerically). However, since every regional minimum, regardless of how tiny and insignificant it is, forms its own catchment basin, this will over-segment the image data. In this study, we use the subnetwork of the over-segmented watershed (SNOW) algorithm proposed by Gostick [17] to reduce over-segmentation issues.

There are two ways to complete pore separation, either directly separating pores or separating grains to achieve the same purpose. Both take almost the same computational time to separate the pore structures of the Berea sandstone in this study, but separating grains has the following shortcomings:

- Separating gains generates more disconnected pore bodies than directly separating pores. For the Berea sandstone under study, separating grains will produce 1494 disconnected pores, while separating pore space generates only 520 pore bodies.
- It is more likely to create pore geometries with small twigs, see **Fig. 2** (a). This may raise a huge computational burden for the surface reconstruction step.
- Some disconnected pores, marked by red circles in **Fig. 2**(a), have no actual solid-pore interfaces.
- Furthermore, separating grains does not provide correct pore connectivity; however, this is the critical information we want

to acquire. This also motivates us to separate pores rather than grains.

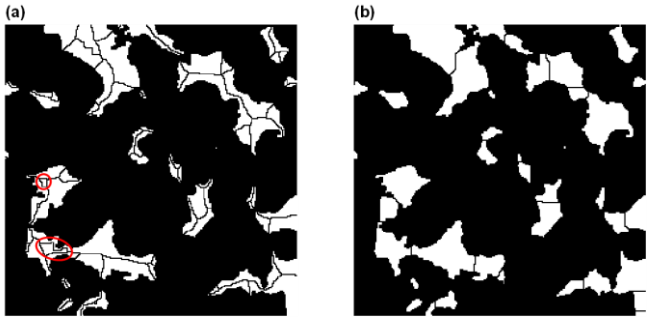

Fig. 2. Pore separation in terms of (a) grains and (b) pores.

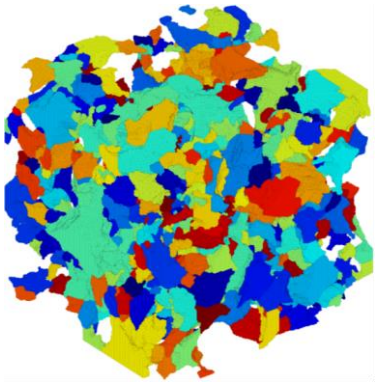

Fig. 3. Disconnected pore geometries of a Berea sandstone by the SNOW algorithm.

Fig. 3 shows the disconnected pores generated by the SNOW algorithm. For illustration purposes, we randomize colors to label different pore bodies after separation. Compared to the original pore structure, the generated pore bodies have simpler geometry, but some of them are still complicated so they cannot be handled by spherical harmonics. In these cases, the second-level pore separation continues by pore skeletonization. **Fig. 4** shows the skeleton of a disconnected pore structure by transparentizing non-skeleton voxels. The blue and red voxels comprise the skeleton, with the red voxels being the nodes that connect two or multiple branches. We utilize the graph theory to find the longest path on which the connections between nodes are selectively broken up to generate child pore structures with reasonable sizes.

Fig. 4. Skeletonization of disconnected pore geometry, with non-skeleton voxels being transparent.

After pore separation, it is important to check whether each individual pore has a spherical topology. If it is not topologically spherical, topology fixing is then applied to repair small vacancies or disconnectivities on the pore surface. This is the prerequisite of spherical parameterization; otherwise the mesh smoothing process fails to continue so that incorrect SH coefficients are calculated. In addition, converting the voxelized pore geometry to triangular surface mesh is found to mildly improve the accuracy, efficiency, and robustness of the surface reconstruction step. Thus, all voxelized pores are converted to surface mesh using iso2mesh [19].

2.3. Pore surface reconstruction

The third step is the key to the success of the proposed workflow by calculating SH coefficients to reproduce the pore surface first. At the very beginning, spherical parameterization is performed to create a bijective mapping between mesh vertices on the pore surface $(x, y, z)^T$ and mesh vertices on the unit sphere surface $(\theta', \varphi')^T$, the latter of which is used to calculate SH basis functions $Y_n^m(\theta', \varphi')$. The initial parameterization usually generates a low-quality mesh, which can significantly reduce the accuracy and efficiency of the subsequent step. Thus, the Control of Area and Length Distortion (CALD) algorithm, proposed by Shen and Makedon [20], is applied here to improve the parameter mesh quality. The CALD algorithm alternately conducts local smoothing and global smoothing: the local smoothing step minimizes the area distortion at a local submesh, while the global smoothing step attempts to equalize the area distortions of the entire parameter surface over the spherical surface.

With spherical parameterization completed, the pore surface can be expressed in terms of SH basis functions

$$x(\theta', \varphi') = \sum_{n=0}^{N} \sum_{m=-n}^{n} c_{xn}^m Y_n^m(\theta', \varphi') \quad (1)$$

$$y(\theta', \varphi') = \sum_{n=0}^{N} \sum_{m=-n}^{n} c_{yn}^m Y_n^m(\theta', \varphi') \quad (2)$$

$$z(\theta', \varphi') = \sum_{n=0}^{N} \sum_{m=-n}^{n} c_{zn}^m Y_n^m(\theta', \varphi') \quad (3)$$

where θ' and φ' are the polar coordinates of vertices on the parameter surface ranging from $[0, \pi]$ and $[0, 2\pi]$ respectively. The real form of the SH function $Y_n^m(\theta', \varphi')$ reads as

$$Y_n^m(\theta', \varphi') = \sqrt{\frac{(2n+1)(n-m)!}{4\pi(n+m)!}} P_n^m(\cos\theta') \cos(m\varphi'), \; m \geq 0 \quad (4)$$

$$Y_n^m(\theta', \varphi') = \sqrt{\frac{(2n+1)(n-|m|)!}{4\pi(n+|m|)!}} P_n^{|m|}(\cos\theta') \sin(|m|\varphi'), \; m<0 \quad (5)$$

and the associate Legendre function P_n^m is given by

$$P_n^m = (-1)^m \left(1 - x^2\right) \frac{d^m}{dx^m} \left[\frac{1}{2^n n!} \frac{d^n}{dx^n} \left(x^2 - 1\right)^n \right]. \quad (6)$$

In the above formulations, n is the index of the SH degree and N is the maximum degree of spherical harmonics. The SH coefficients c_{xn}^m, c_{yn}^m, and c_{zn}^m are solved using the standard least squares algorithm, since the number of equations is often greater than the number of unknowns. **Fig. 5** (b) shows the reconstructed pore surface, represented by the green surface with grey lines. It captures the surface textures of its voxelized pore geometry, as shown in **Fig. 5** (a).

(a) **(b)**

Fig. 5. Voxelized pore structure (a) and reconstructed pore surface (b) (green surface with grey lines). The reference surface is plotted with a semi-transparent surface and blue lines, overlapping with the reconstructed surface.

2.4. Roughness evaluation and parameterization

In the last step, we need to create the reference surface to define and characterize "surface roughness". Since the morphology of the reconstructed surface is controlled by the number of SH series, reducing the series expansion gradually removes the surface textures; at the end only the general pore shape is preserved. In this study, we set the total degree $N = 4$ so that 16 spherical harmonics are used to build the reference surface. The local roughness is defined by the shortest distance from mesh vertices of the reference surface to the pore surface. **Fig. 6** shows the distribution of local roughness mapped to the reference surface. The cold and warm color represent that the reference surface lies above and below the pore surface, respectively.

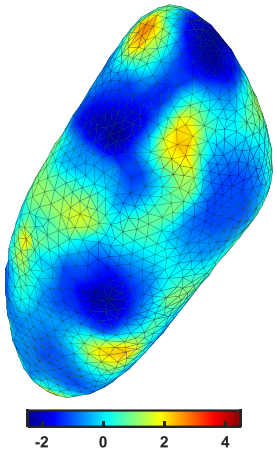

Fig. 6. Distribution of local roughness over the reference surface.

Eventually, the 3D surface roughness is parameterized as a single number by calculating the average of the local roughness weighted by the control area of each mesh vertex on the reference surface, as shown by **Eq. 7**

$$R = \frac{\sum_i h_i \hat{a}_i}{A_{\text{total}}} = \frac{h_1\hat{a}_1 + h_2\hat{a}_2 + h_3\hat{a}_3 + h_4\hat{a}_4 + \cdots}{A_{\text{total}}} \quad (7)$$

where h_i is the local surface roughness at ith vertex, $\hat{a}_i$ is the controlled area of ith vertex delineated by the blue line in **Fig. 7**, A_{total} is the total area of the reference surface.

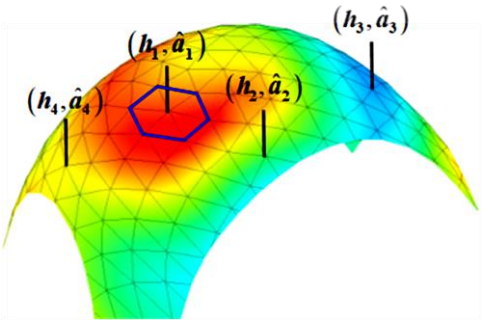

Fig. 7. Schematic diagram of surface roughness parameterization. The blue curve delineates the control area of a vertex on the reference surface.

3. Numerical results

The effectiveness of the proposed workflow is illustrated by characterizing 3D pore surface roughness of a Berea sandstone. The rock image is downloaded from the Pore-Scale Modelling and Imaging group at Imperial College London. The image size is $256 \times 256 \times 256$ with the resolution of 2.7745 um.

After dividing the connected pore structures, a morphological opening and a hole-filling operation are applied to remove some surface defects caused by the first-level pore separation. This increases the robustness of the surface reconstruction step at a slight compromise in accuracy. In this study, the maximum degree of spherical harmonics is fixed at 40. The maximum number of iterations for local and global smoothing in spherical parameterization is 10 and 100, respectively.

As surface triangulation is suggested as the input rather than voxelized pore geometry to the surface reconstruction

step, we first investigate their influence on the performance of surface reconstruction. Compared to the mildly smoothed triangular mesh, the voxelized pore geometry has many angular corners that affects the calculation of SH coefficients to reproduce the pore surface. **Fig. 8** shows an example of (a) voxelized pore geometry, (b) reconstructed surface based on (a), and (c) reconstructed surface from a mildly smoothed surface mesh. As shown in **Fig. 8** (b), with voxelized pores as input, spherical harmonics attempt to reproduce the sharp corners, resulting into a poor-quality surface mesh. From the perspective of computational efficiency, this example (around 17000 pore voxels) does not show a distinct difference either using voxelized or mesh data as input. However, as the pore size becomes larger, the number of vertices and faces of voxelized pore geometry increases a lot. This means that the spherical parameterization step has to take more time to smooth the mesh of parameter surface and the spherical harmonic expansion has to solve a larger linear system. Through our numerical tests, reconstructing a pore geometry with more than 45000 pore voxels doubles the computational time of surface reconstruction using triangular surface mesh.

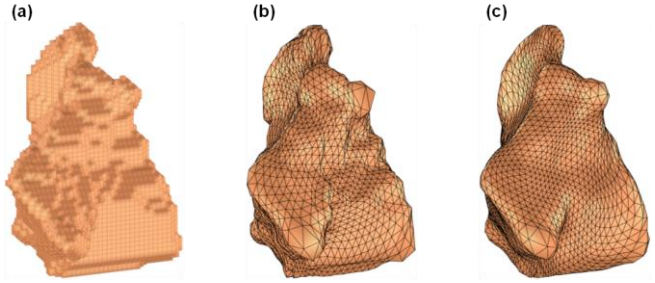

Fig. 8. Comparison of voxelized pore structure (a) with reconstructed surfaces by voxelized pore geometry (b) and triangular surface mesh (c).

Then a robustness test is conducted to examine whether the proposed approach works for elongated or plate-like pores. A few plate-like pores are separated from the Berea sandstone, and none of elongated pores is found. **Fig. 9** (a) shows a plate-like pore, with flatness and elongation being 0.5722 and 0.1192, calculated using the formulation proposed by Angelidakis et al [21]. We calculate the relative errors of volume enclosed by the reconstructed surface, surface area, and shape factor, with respect to corresponding values of the surface triangulation, to quantify the accuracy of the pore surface reconstruction. The relative errors of volume, area and shape are 0.6012, 0.5246 and 0.3711 respectively, indicating the proposed approach enable to handle plate-like or elongated pores without computational difficulty.

Fig. 9. Illustration of a plate-like pore: (a) voxelized geometry, (b) surface triangulation, and (c) reconstructed pore surface. The flatness and elongation are 0.5722 and 0.1192, respectively.

Fig. 10, **Fig. 11**, and **Fig. 12** show surface roughness characterization for three separated pores. From top to bottom, three voxelized pore structures exhibit visually increasing surface roughness. The last column of **Fig. 10** to **Fig. 12** shows the distribution of local roughness calculated from **Eq. 7**. However, not all of the measurements contribute to the surface roughness evaluation, since some vertices are on dummy surfaces ("skin") that do not belong to the solid-pore interface, as shown in **Fig. 13** (a). To improve the accuracy of surface roughness estimates, we first iterate mesh vertices on the reference surface and check if any vertex is on the skin or if its normal vector passes through the skin. These vertices, shown as red dots in **Fig. 13** (b), will be removed from surface roughness parameterization. After calibration, the surface roughness coefficients from **Fig. 10** to **Fig. 12** are 0.5852, 1.5396, and 4.2588.

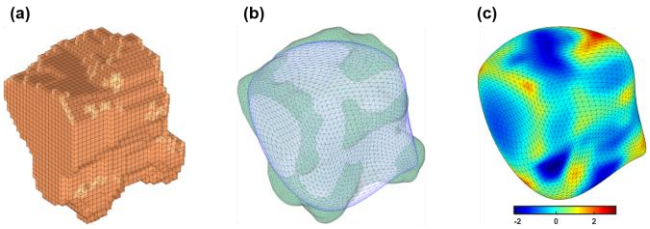

Fig. 10. Illustration of pore 73: (a) voxelized pore geometry, (b) pore (green color with grey lines) and reference surface (white color with blue line), and (c) local roughness distribution.

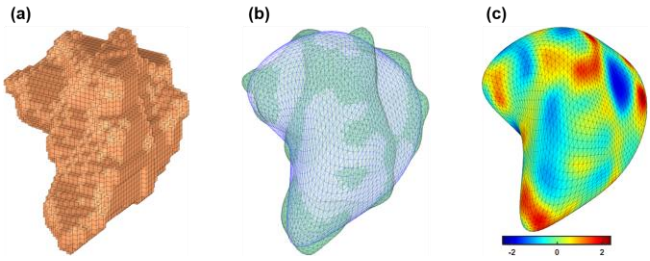

Fig. 11. Illustration of pore 56: (a) voxelized pore geometry, (b) pore and reference surface, and (c) local roughness distribution.

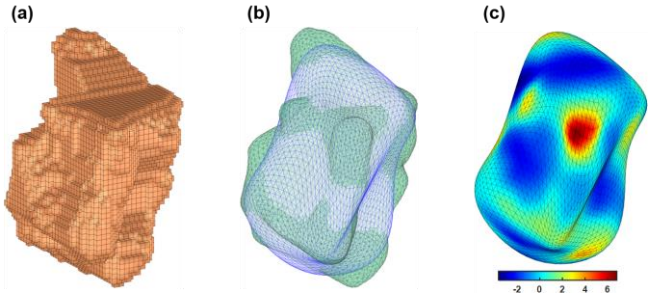

Fig. 12. Illustration of pore 127: (a) voxelized pore geometry, (b) pore and reference surface, and (c) local roughness distribution.

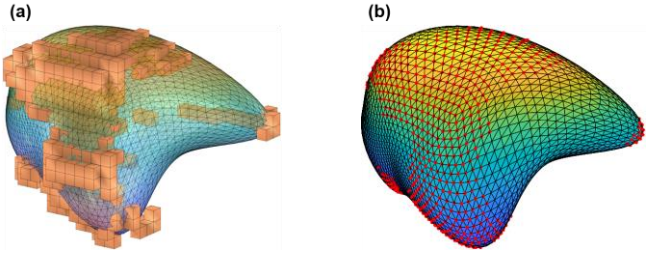

Fig. 13. Determination of (a) intersection of the reference surface and dummy surfaces and (b) mesh vertices (marked as red dots) that are not involved in surface roughness parameterization.

Fig. 14 shows the relative errors of volume, surface area, and shape factor of the reconstructed pore surface with respect to the corresponding values of input surface mesh. Overall, the reconstructed surface preserves high accuracy, which guarantees SH coefficients are properly calculated to create the reference surface. **Fig. 15** shows the distribution of surface roughness coefficients of separated pore geometries for the Berea sandstone. More than 80% of separated pores have surface roughness coefficients smaller than 2. The average of surface roughness coefficients is around 1.4472, which is smaller than the average roughness reported in [2]. There are two reasons that can account for the difference. First of all, the reported results in [2] is measured from high-resolution images. Thus, more fine-scale surface textures can be resolved, which will increase the surface roughness estimation. Second, Ma et al. [2] utilized the laser scanner confocal microscope to conduct high-precision surface roughness measurements. The measured data are processed by filtering out the pore-shape/pore-size effect, while in this study the pore-shape effect is regarded as "surface roughness" from the macroscopic point of view. Even though their measurements are the "actual" roughness (surface textures visible at higher resolution), these data are measured from a 2D cross-sectional plane of the given rock sample and they may not fully represent the surface roughness in 3D space. Overall, the proposed method provides a technologically feasible approach to characterize the pore surface roughness at the micrometer scale, which can benefits to accurate evaluation of pore structures from NMR T2 relaxation simulation.

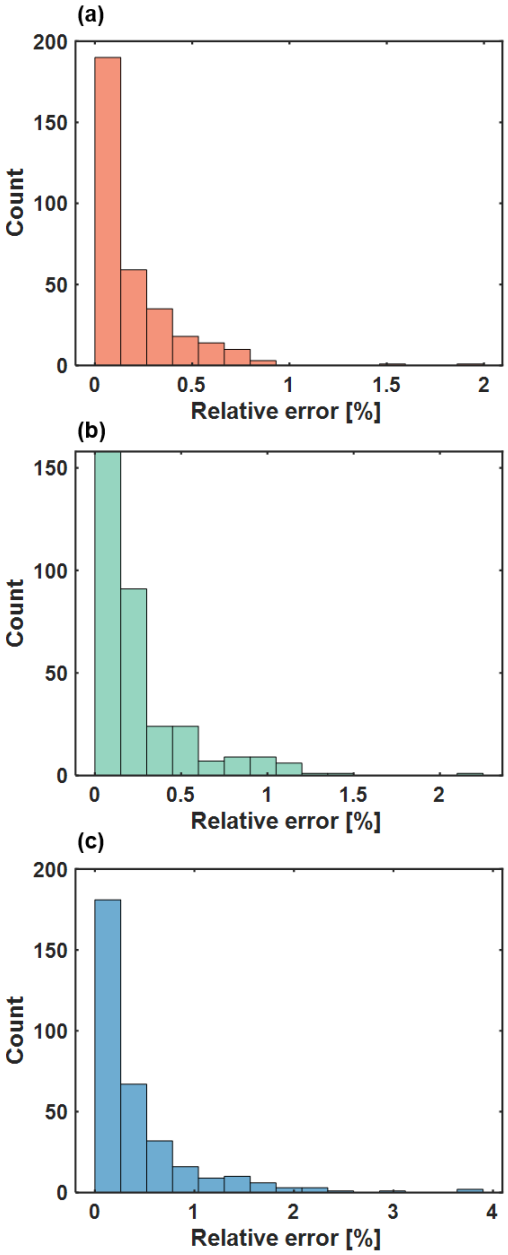

Fig. 14. Relative errors of volume, surface area, and shape factor for all separated pores.

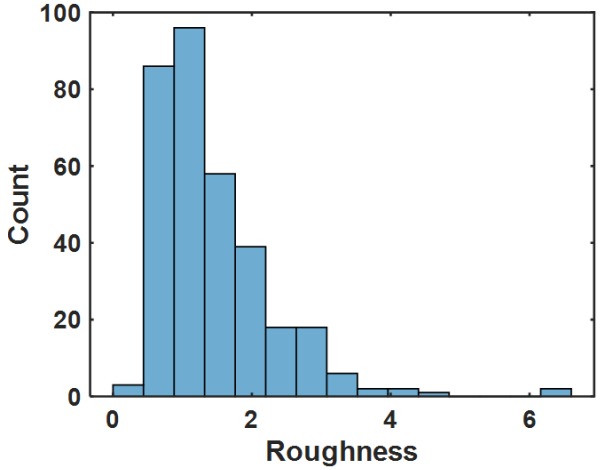

Fig. 15. Distribution of surface roughness coefficients of separated pores from the Berea sandstone under study.

4. Conclusion

This study develops an image-based workflow utilizing spherical harmonics to characterize pore surface roughness from segmented μ-CT images. To ease surface roughness characterization, the connected pore structures are divided into a plurality of disconnected pores using a two-level pore separation algorithm. Then use the combination of spherical parameterization and spherical harmonic expansion is used to calculate SH coefficients by fitting the surface mesh of pore bodies, and build the reference surface to quantify 3D pore surface roughness. The calculated 3D roughness coefficients agree with the visual inspection of pore geometries. Moreover, the average of calculated 3D surface roughness coefficients is consistent with the reported values to some extent. The proposed approach provides a technologically feasible approach to characterize 3D pore surface roughness characterization at the micrometer scale.

Acknowledgments

We would like to thank Saudi Aramco for funding this research. We would also like to thank King Abdullah University of Science and Technology (KAUST) for providing a license for MATLAB.

References

1. N.R. Morrow, J. Can. Pet. Technol. **14**, (1975).
2. S.M. Ma, G. Singer, S. Chen, M. Eid, SPE J. **26**, 2860 (2021).
3. G.R. Coates, L. Xiao, M.G. Prammer, *NMR logging: principles and applications*, (1999).
4. K.R. Brownstein, C.E. Tarr, Phys. Rev. A **19**, 2446 (1979).
5. S. Kruschwitz, M. Halisch, R. Dlugosch, C. Prinz, Geophysics **85**, MR257 (2020).
6. G. Singer, S.M. Ma, S. Chen, M. Eid, *2D Surface Roughness Quantification for Enhanced Petrophysical Applications*, (OnePetro, Houston, 2022).
7. Y. Li, X. He, M. AlSinan, E. Ugolkov, H. Kwak, H. Hoteit, *Numerical Study of Surface Roughness Influence on NMR T2 Response*, (EAGE, Madrid, 2022).
8. Y. Li, M. Alsinan, X. He, E. Ugolkov, H. Kwak, H. Hoteit, *NMR T2 Response in Rough Pore Systems: Modeling and Analysis*, (OnePetro, Houston, 2022).
9. C.H. Arns, A.P. Sheppard, R.M. Sok, M.A. Knackstedt, Petrophys. **48**, (2007).
10. O. Talabi, S. Alsayari, M.A. Fernø, H. Riskedal, A. Graue, M.J. Blunt, *Pore-scale simulation of NMR response in carbonates*. (SCA, Abu Dhabi, 2008).
11. L. Shen, F. Makedon, Image Vis. Comput. **24**, 743 (2006).
12. C. Brechbühler, G. Gerig, O. Kübler, Comput. Vis. Image Underst. **61**, 154 (1995).
13. G. Gerig, M. Styner, D. Jones, D. Weinberger, J. Lieberman, *Shape analysis of brain ventricles using spharm*, (IEEE, Kauai, 2001)
14. L. Shen, J. Ford, F. Makedon, A. Saykin, Intell. Data Anal. **8**, 519 (2004).
15. L. Shen, H. Farid, M.A. McPeek, Evol. **63**, 1003 (2009).
16. A. Rabbani, S. Jamshidi, S. Salehi, J. Pet. Sci. Eng. **123**, 164 (2014).
17. J.T. Gostick, Phys. Rev. E **96**, 023307 (2017).
18. D. Kong, J. Fonseca, Géotechnique **68**, 249 (2018).
19. Q. Fang, D.A. Boas, *Tetrahedral mesh generation from volumetric binary and grayscale images*, (IEEE, Boston, 2009)
20. L. Shen, F. Makedon. Image Vis. Comput. **24**, 743 (2006).
21. V. Angelidakis, S. Nadimi, S. Utili, Powder Technol. **396**, 689 (2022).